

Numerical Modeling of Tidal Effects in Polytropic Accretion Discs

David Goden

Jet Propulsion Laboratory
California Institute of Technology
4520 Oak Grove Dr., MS 288-647
Pasadena, CA 91109
e-mail: goden@berca.jpl.nasa.gov

Received [date]

Abstract

A two-dimensional time-dependent hybrid Fourier-Chebyshev method of collocation is developed and used for the study of tidal effects in accretion discs, under the assumption of a polytropic equation of state and a standard alpha viscosity prescription. First a cool disc with a steady mass inflow at the outer radial boundary is assumed to model discs in S_{1/2}V₀, a sub-class of Cataclysmic Variables. For mass ratios in the range $\eta < 0.1$, calculated toroidal effects induce $m = 1, 2$ azimuthal modes in the disc. The $m = 2$ mode consists of a double spiral density pattern in the whole disc, and a precessing elliptic density pattern in the very inner part of the disc. The $m = 1$ mode is characterized by a rotating crescent in the inner disc, which generates a wave that propagates outward into the whole disc and induces an eccentric motion of the double spiral pattern. The initial growth of the eccentric mode is exponential. Within the evolution time considered here, the $m = 1$ mode grows to a value comparable to the eccentric motion of the disc, the amplitude remaining constant in the inner part of the disc, but decreasing in the outer part of the disc.

We also find that the effect of tidal forces on the disc is to produce a double spiral density pattern, dissipating power in the disc, and to excite low and high density regions rotating at the local Keplerian frequency, where the CVs and NSOs turn out to be non-axisymmetric at small radii. This long-period mode is generated by a tidal torque, very similar to the one occurring in pulsating white dwarfs. We also find that the disc exhibits oscillations observed in the inner part of discs, and the periods of the open system with the inclusion of quasi-periodic and coherent oscillations discussed in Cataclysmic Variables.

Subject: Cataclysmic variables; accretion discs; hydrodynamics; plasma theory; methods: numerical; stars: neutron; stars: pulsars; stars: variables.

1 Introduction

Tidal interaction of discs with an orbiting exterior companion has received recently some attention because it is believed to be responsible for two different important processes in planet formation: In hot discs it can transport angular momentum (Savonije, Papaloizou & Lin 1994; for a review of angular momentum transport in discs see Pringle 1994, Livio 1995), and in discs with a low-mass companion it can induce eccentricity growth (Ushiro 1991a & b). The two different classes of objects are observable stellar systems. The transport of angular momentum is believed to take place in Young Stellar Objects, where a protoplanetary disc is perturbed by a giant protoplanet; and in S \star 1 Ma sub-class of Cataclysmic Variables the tidal resonance induces eccentricity growth in the disc.

The main interaction between the disc and the companion is through tidal resonance. The matter in the disc at certain radii has an orbital period $P = P_0$, which is a factor $\omega = \Omega/\omega_0$ away from the 'local' Keplerian period $P_0 = 2\pi/\Omega_0$. These radii are resonance radii (an orbiting test particle at a distance r from the centre of the disc has a period $P = 2\pi r^{\frac{3}{2}}/\Omega_0$). The corresponding resonance condition is $\omega = \Omega/r^{\frac{1}{2}}$. The radius r is the 'resonance radius' and ω is the 'resonance frequency'. The angle θ is the 'resonance angle' (it is measured from the direction of the orbital motion to the direction of the wave propagation) denoted around at the resonance radii. Due to the effect of the resonance, the matter in the disc is wound up into spiral patterns and matter moves into the disc at roughly the sound speed c_s , i.e. wound-up in the angular direction at roughly the 'local' Keplerian speed. One figure precisely at the 'local' rotation rate Ω_0 . As the resonance frequency is roughly equal to the rotation rate in the disc, the right angle between the local speed of the test particle and the disc ('the tangent of the angle can be written

$$\tan \theta = \frac{c_s}{\Omega_0 r} = \frac{M}{r^{\frac{3}{2}}} \quad (1)$$

We are interested in the behaviour of the angle θ in the radial range of the disc, i.e. the innermost and outermost parts of the disc, and the outermost disc, i.e. the outermost part of the disc, where the matter has been completely decelerated from Keplerian motion. This is the case in the inner region of the disc, where it will wind up roughly at $\omega \approx M/2r$ (since when it reaches the inner region of the disc, $\omega_0/2$ denotes the 'resonance' angular velocity in the disc). In fact there $(M \approx 10^{-3}$ solar stars) $\omega \approx 1$, where in cool discs $M \approx 10^{-10}$ CV systems $\omega \approx 8$. Therefore, in cool discs the wave has to propagate over a much longer

distance and dissipates 'mainly through shocks and viscous effects' before it reaches small radii. One can also define the wavelength λ in the radial direction $\lambda_l \approx \Delta r/l \approx 2\pi H/l$ and a wave number $k \approx l/H \approx \Omega/c_s$. As the wavelength decreases (k increases as r decreases) it becomes small compared with the scale associated with the forcing potential (Savonije, Papaloizou & Lin 1994) and the waves cannot reach small radii (for a detailed review and a rigorous treatment see Lin & Papaloizou 1993). The angular momentum is transported in the disc in the following manner. The matter in the disc rotates at about the Keplerian velocity and 'collides' with the high density spiral pattern which rotates with the binary. As a consequence, the disc 'loses' angular momentum, which is gained by the companion, and the matter in the disc drifts further inward. Therefore, one expects tidally induced accretion to be important in hot discs, where it can provide an alternative to the ad-hoc alpha viscosity prescription. In cool discs tidal effects will not affect significantly the accretion rate, because of the high Mach number, but the tidal resonance can induce eccentricity growth. When the mass of the companion is low, the outer edge of the disc reaches the 3:1 resonance radius $r = 3r_{\text{res}}$ (or eccentric 3:2 tidal resonance). Now, if any small 'perturbation' (e.g. tidal or ellipticity effects in the disc) is introduced, 3:2 'pitchfork resonance' will tend to increase the eccentricity. This is the reason why the tidal resonance leads to $\omega = 3$ in the opposite 'pitchfork resonance' (see Savonije 1994).

Resonances under various assumptions. Tidally induced angular momentum transport in discs was modelled by Savonije et al. (1994, see also the references therein), who showed that angular momentum transport occurs efficiently in hot discs, but is negligible in cool discs. The interaction of a giant extrasolar planet with the protoplanetary disc was studied analytically and numerically (with a relativistic code) by Lin & Papaloizou (1992), considering several important issues such as the migration of the planet, the formation of a gap, and the fate of the disc when it becomes an entropic disc, with no mass inflow at the outer edge of the disc, and orbital eccentricity (and hence tidal) instability solutions with spiral patterns from $\omega_0 = 2, 3, 4$ (long spiral resonances). On the other hand, Smoothed Particle Hydrodynamics (SPH) and other particle methods for simulations of tidally excited discs (Lin & Murray 1994, for a recent review see Murray 1996, and the references therein). Their results show an eccentric disc which makes a long pitchfork resonance in the inertial frame of reference. The stream of matter from L_0 tends to circularize the disc orbits and inhibit the disc radial expansion (Murray 1996). The spiral pattern is seen only in the far outer part of the

disc. The eccentricity is caused by the 3:1 tidal resonance instability (Lubow 1992), and provides an explanation of the superhump phenomena observed in SU UMa CVs (Vogt 1982; see also Osaki 1994). These results were not reproduced by usual finite difference methods (e.g. Lin & Papaloizou 1993).

Rójczyk & Sieniut (1993) carried out numerical simulations with a more refined code. They used an inviscid code including basic cooling processes and mass transfer from the companion, and obtained no eccentric disc at all. Instead, the mass transfer accumulates into a ring which eventually becomes unstable and is accreted onto the central object, providing therefore a new interesting mechanism for outbursts in CVs. The accretion through tidal torque is not uniform through the disc: it is higher in the outer part of the disc, where shocks usually appear. Consequently, mass transfer in the outer disc is higher than in the inner disc, and mass accumulates in a ring until it becomes unstable. Rójczyk & Sieniut (1993) used a realistic model, but overestimated the temperature of the disc in CVs (their density is too large by a factor of 100), and the Mach number in the disc is around 10 instead of 100, and the angular velocity is roughly 10 times of that in CVs (100°/s instead of 10°/s). Some authors (see below) give the flow parameters

$$f_{\text{outer}} \approx 100, f_{\text{inner}} \approx 10,$$

and density 100 times lower than in CVs. A very strong dependence of the disc properties on the flow parameters has been shown by Perna & Deeg (1992). Clearly, the differences between the results of the present work and those of others (not cited here) is due mainly to the different assumptions made on the mass inflow and the viscosity (the different numerical methods also have different local properties and resolutions).

In the present work, we use a two-dimensional time-dependent polytropic spectral code to study tidal effects in a disc or flow. We assume a standard disc viscosity prescription. We consider dimensionless variables and around Noyau Stellar Unipole. First, we consider a quasi-axisymmetric disc only an $m = 0$ azimuthal mode corresponds to the steady state with a steady mass inflow and a steady radial torque due to tidal effects in CVs. In this case the viscosity of the disc is small enough to consider that the mass is accreted in the inner part through various disc states. For a mass ratio q in the range $0.001 < q < 0.1$ (calculated here), tidal effects induce $m = 1, 2$ modes in the very inner part of the disc. The $m = 2$ mode is characterized by a precessing elliptic density pattern with a period shorter than the binary orbital period but longer than the local Keplerian period. The $m = 1$ mode consists of a rotating crescent (with a period slightly larger

than the binary period) which induces a slightly eccentric motion of the spiral pattern. However, within the evolution time considered here ($t \sim 10^4$), the $m = 1$ mode is unable to disrupt the flow into a completely eccentric precessing disc. Then we consider a hot disc with no mass inflow to model protoplanetary discs in VSOs. We assume the disc to be viscous but with a lower value of alpha ($\alpha = 0.01$). In this case we use an 'isothermal' version of the code. Here also a double spiral pattern forms after one binary period. As the matter in the disc drifts inward, the density increases in the inner disc, while the tidal interaction in the outer disc weakens, and the spiral pattern dissipates. The density distribution exhibits a low order mode ($m = 2$) in the very inner disc, which is identified as low and high density regions rotating at the local Keplerian velocity. Both the CVs and VSOs discs are now axisymmetric at small radii, with irregular patterns rotating at about the local 'Keplerian speed'.

In the following section we write down the governing equations of the flow together with the physical parameters. In the next section we present the numerical method and the numerical results. Finally, we discuss the physical consequences of our numerical results.

2. $\nabla \leq 3$ and Assumptions

2.1. The Equations

The problem considered here consists of a disc of matter surrounding a compact body (the gravitation of a secondary star or a planet) in a circular orbit. The external force applied to the disc is the mass inflow due to tidal torques. The self-gravitation of the disc is neglected. The viscosity in the disc is due to turbulent viscosity, rotation and thermal conduction effects. The governing equations are the Navier-Stokes equations written in spherical coordinates (r, θ) , see for example, Perna & Deeg (1992) for details. The disc rotates in the same direction as the binary system, and the rotation is slow compared with the orbital motion. The disc is assumed to be axisymmetric, and the flow is considered to be steady. The disc is considered to be thin, so that the vertical coordinate z is assumed to be small. The equations are written for the density ρ and the momenta $P = p_r, P_\theta$ and $H = \mu_{\theta r}$ in the following manner:

$$\frac{\partial \rho}{\partial t} + \frac{1}{r} \frac{\partial}{\partial r} \left[r G(f) + \frac{\alpha}{r} H(f) + S(f) \right] = 0,$$

where the coordinate r and the flux vector is \mathbf{G}_r , have

$$\mathbf{f} = \begin{pmatrix} \rho \\ W \\ H \end{pmatrix}, \quad \mathbf{G}(\mathbf{f}) = \begin{pmatrix} \frac{\partial}{\partial r} + P - R_{\theta\theta} \\ \frac{\partial}{\partial r} + R_{\theta\theta} \\ \frac{\partial}{\partial r} + P + R_{\theta\theta} \end{pmatrix}, \quad \mathbf{H}(\mathbf{f}) = \begin{pmatrix} \frac{\partial}{\partial r} + R_r \\ \frac{\partial}{\partial r} + R_{\theta\theta} \\ \frac{\partial}{\partial r} + P - R_{\theta\theta} \end{pmatrix}$$

and the vector field \mathbf{S} is defined according to

$$\mathbf{S}(\mathbf{f}) = \begin{pmatrix} 0 \\ \frac{\partial}{\partial \theta} - \frac{W^2}{r} - \frac{R_{\theta\theta}}{r} - \rho \frac{\partial V}{\partial r} \\ \frac{\partial}{\partial \theta} + \frac{R_{\theta\theta}}{r} + \frac{\rho}{r} \frac{\partial V}{\partial \theta} \end{pmatrix}$$

The momentum transport terms in \mathbf{S} is defined by

$$2H_{\text{max}}\rho = \int_{-H_{\text{max}}}^{H_{\text{max}}} \rho(z) dz = \int_{-\infty}^{\infty} \rho(z) dz = \Sigma$$

where H_{max} is an integration radius (see also Godon et al., 1995; Godon & Lignières, 1997), the two bodies of masses M and m rotate: $a_r = \omega r$ is the orbital velocity, V is the gravitational potential and Ω is the angular velocity of the stars.

18

where we have neglected small terms which include $\partial/\partial\phi$ derivatives. A star's spin velocity Ω is equal to the coefficient of the viscosity S times the star's spin period:

$$\Omega = S \cdot \Omega_{\text{period}}$$

where S is a constant of rotation and $\Omega_{\text{period}} = 2\pi/P$ is the period, where P is the spin period. The viscosity coefficient S is proportional to the square of the shear modulus G and the density ρ .

The viscosity S is given by the following expression in terms of

2.2 Physical assumptions

The equations are solved in the rotating frame of reference of the binary system. Therefore, the source term in equations (2) includes the Coriolis and the centrifugal forces:

$$\mathbf{S} = \begin{pmatrix} 0 \\ \frac{\partial}{\partial r} + \frac{W^2}{r} - \frac{R_{\theta\theta}}{r} - \rho \frac{\partial V}{\partial r} + 2\omega W - \rho \omega^2 r - a_r \cos \phi \\ -\frac{\partial}{\partial \theta} + \frac{R_{\theta\theta}}{r} + \frac{\rho}{r} \frac{\partial V}{\partial \theta} - 2\omega l + \rho \omega^2 a_r \sin \phi \end{pmatrix}$$

The distance between the two stars is denoted by a and ω is the angular rotation rate of the binary.

$$\omega = \frac{(GM + m)^{1/2}}{a^3}$$

a_r is the distance of the primary star from the center of mass of the system around which the two bodies (of masses M and m) rotate: $a_r = \omega r / (\omega M + \omega m)$. V_0 is the gravitational potential and Ω is the angular velocity of the primary star. The initial condition of \mathbf{f} is the gravitating collapse of

19

$$V_0 = -\frac{Gm}{r^2 + a^2 - 2ra \cos \phi/2}$$

In the polytropic equation of state, the polytropic index is $n = 5$ and the polytropic constant is given by

$$\gamma = \frac{2\alpha}{n-1}$$

where α is the initial density at $r = R_{\text{init}}$ and ϵ is a small parameter related to the radial thickness of the disk: $r = R + \epsilon H$ at the outer boundary R_{out} . The polytropic constant is given by $\alpha = 3/2$ and $\gamma = 5/3$.

2.3 Boundary and. Initial conditions

Since there are two second order equations (the momentum equations) and one first order equation (the density equation), a total of five boundary conditions have to be specified (two conditions for the momenta at each boundary, and one condition for the density at one boundary). The conditions are imposed on the inflowing characteristics of the flow at the boundaries (see section 3.4). When working with the spectral methods, one has to be very careful to impose the boundary conditions on the characteristics of the flow and not to over specify any variable at the boundaries. The inner boundary of the computational domain is located at $r = R_{in}$. At this boundary $\Omega = v_0/r$ is given by equation (6), and we impose one of the three following conditions: $v_r = 0$, $U = p_{r\theta} = U_0$, or $\partial U/\partial r = 0$. The outer boundary of the computational domain is located at $r = R_{out} = 5R_{in}$ and is a boundary through which matter can flow. We impose there three conditions, one on each variable. On p_r , $\partial p_r/\partial r = 0$; on U , $U = U_0$; and on Ω , $\partial \Omega/\partial r = 0$ or Ω given. We tried different boundary conditions, and the exact conditions imposed in the literature for each model are summarized in the following.

For the linearized equations of state, the initial conditions are $\Omega = \text{constant}$, $v_r = 0$, $U = U_0$, $p_r = p_{in}$, and $\partial p_r/\partial r = 0$.

$\partial/\partial t = 0$ and neglecting the terms which include v_r and $\partial P/\partial r$ (this is a good approximation when $v_r, v_\theta \ll c_s$, which holds for thin discs where $c_s \ll U_0$),

$$\frac{\partial \Omega}{\partial t} = \frac{\partial \Omega}{\partial r} + \frac{\partial^2 \Omega}{\partial r^2} - u_r^2/c_s^2 \cos^2 \phi + u_\theta^2/c_s^2 = 0. \quad (5)$$

The physical solution of this equation

$$\Omega = -\frac{c_s^2}{r^2} + u_r^2 \cos^2 \phi$$

is used as initial condition for the Chebyshev expansion in the radial direction. The initial radial velocity $v_r = 0$. The modes are evolved in one dimension at $\phi = 0$ and $\partial/\partial \phi = 0$, and after a few many orbital periods their evolution is followed in two dimensions. This procedure slightly reduces the computational time needed and provides good initial conditions for the two-dimensional problem. In some cases it also helps to avoid numerical instabilities which occur during the initial relaxation of the two-dimensional mode's.

3 The numerical method

We treat the spatial dependence of the equations with a hybrid Fourier-Chebyshev Spectral method (Gottlieb & Orszag 1977, Voigt et al. 1981, Canuto et al. 1988), while an explicit fourth order Runge-Kutta method is used for the time dependence of the equations. The Chebyshev pseudospectral method is used in the radial direction (Godon et al. 1995 and Godon 1995, 1998a & b), and is appropriate for nonperiodic boundary conditions. The partition of the grid points is higher at the boundaries. In the azimuthal direction a Fourier expansion is used, appropriate for periodic boundary conditions. The Fourier expansion $e^{im\phi}$ is an ideal basis to represent the azimuthal mode ($m = 0, 1, 2, \dots$) of the flow, and a small number of terms should be enough. Fourier expansions are suitable to represent small amplitude waves which are obtained in the limit of a linearization of the equations in first order perturbation theories. In the non-linear regime, the waves can no longer be represented by sinusoids, and a large number of terms is required to represent a single wave. This is the reason that the option n_m in eqn. 10 is set to 1000, whereas n_r is set to 100 for the computation of the linearized equations (see section 3.3).

3.1 The Chebyshev Spectral Method

The Chebyshev method of calculation is based on the Chebyshev polynomials of the first kind, defined by the recurrence relation $T_0(y) = 1$, $T_1(y) = y$, and

$$T_N = \sum_{n=0}^N a_n T_n^N. \quad (6)$$

where the Chebyshev coefficients are given as

$$a_n = \frac{2}{\pi} \int_0^\pi T_N(\cos \theta) \cos(n\theta) d\theta = (-1)^{n+1} \frac{(-1)^n}{n+1}. \quad (7)$$

$$T_N = \sum_{n=0}^N a_n T_n^N. \quad (8)$$

$y_1 = \cos(\pi j/N)$, $j = 0, 1, \dots, N-1$, and $a_0 = a_N = 1$, $a_1 = 0$, $a_2 = 1/2$, ..., $a_{N-1} = (-1)^{(N-1)/2}$. The expression for T_N can be

$$\frac{d^N y}{dy^N} = \sum_{n=0}^N a_n T_n^N(y). \quad (9)$$

and now

$$\frac{d\delta_N}{dy} = \sum_{n=0}^{N-1} c_n^T T_n$$

The recurrent relations between $T_n(y)$ and $T_n(p)$ leads to the following rule:

$$c_n^T = \frac{2}{\pi} \sum_{n=p+1}^{N-1} p a_{n+1} \quad (10)$$

where $a_0 = 2$, $a_j = 1$ for $0 < j < N$ and $p=n+1/2$ means $p=n+1/2, \dots, N-1$. This can also be computed with the following fast algorithm:

$$\begin{aligned} C_{N,N}^T &= n \\ \sqrt{2} N_{N-1}^T &= \\ \sqrt{2} a_n^T &= \frac{1}{\pi} (a_{n+1} + 2(n+1)a_{n+2}), \quad n = N-2, \dots, 0 \end{aligned}$$

In the present work, the code is implemented by using a modified Chary-Chen Method of Collocation developed by Trefethen (1982). The main steps are given:

$$\begin{aligned} \text{Step 1:} & \quad \text{Divide } [R_{in}, R_{out}] \text{ into } N \text{ subintervals} \\ & \quad \text{Let } \Delta r = \frac{R_{out} - R_{in}}{N} \end{aligned}$$

The α parameter is set to 1, and the grid points are distributed according to the boundary condition $\sigma = 1$ and $\sigma = -1$, respectively. When $\alpha = 1$ the grid points are distributed symmetrically in the interval $[R_{in}, R_{out}]$, and when $\alpha = -1$ the grid points are concentrated near the outer boundary. The collocation points are sampled at n and $n+1/2$ (the so-called "Moulton method" ($\Delta r \approx \Delta N$)). In this way, the innermost and outermost grid points are located at $y \approx N \Delta r$ and $y \approx N \Delta r + \Delta r/2$ when the α parameter is set equal to one or minus one. However, it is important to stress that in order to obtain a stable solution, one needs to have a large number of grid points is kept close to the boundaries. This insures that the boundaries are treated with a high accuracy. Moreover, the overall accuracy decreases

as α , β increase (Kosloff & Tal-Ezer 1993). We write $\alpha = \cos(s\pi/N)$, and $\beta = \cos(p\pi/N)$, where $s = (N-1)/n_s$, and $p = (N-1)/n_p$, and then chose n_s and n_p in the range 2–9. For each model their exact values are specified in the results section. In the present calculations this increases the time step by a factor of up to 7 for $N = 64$. The derivative is then calculated using the chain rule:

$$\frac{df}{dx} = \frac{1}{g'(y; \alpha, \beta)} \frac{df}{dy}, \quad (11)$$

where

$$\frac{1}{g'(y; \alpha, \beta)} = \frac{n}{\sqrt{\alpha \beta}} \sqrt{(1-\alpha y)(1+\beta y)}, \quad (12)$$

and the derivative df/dy is obtained using the relations (10-11).

The following coordinates transformation is then made $r = (x+1) + R_{in}$ and the unit of length in the equations is chosen such that $R_{out} = R_{in} + 2$, where R_{in} and R_{out} are the location of the inner and outer radial boundaries respectively.

An exponential basis function is used in the radial direction and the radial coordinates are converted into an exponential grid interval referred to as "Cartesian". That is, $x = \ln(r) - \ln(R_{in})$ and the radial grid points are distributed in the following manner:

at x_{in}, R_{in} :

$$e^{N_x} \leq \sigma \leq e^{N_x},$$

where

$$0 \leq \sigma \leq N_\sigma,$$

at

$$e^{N_x} \leq \sigma \leq N_\sigma, \quad N_x < \sigma < N_\sigma.$$

The values of N_x , σ and N_σ must be determined for each coordinate and are found by trial. The value of N_x must be big enough so that not too many grid points fall outside the interval $e^{N_x} \leq \sigma \leq N_\sigma$ (for example, in the beginning of the calculation, $N_x = 0$). The N_σ value is determined by the requirement that the grid points are distributed uniformly. In the present calculations we chose $N_x \approx 5N_\sigma$, $\zeta = 4$ and $\eta = 2$.

3.2 The Fourier Method of collocation in ϕ

A Fourier expansion is carried out in a similar way in the azimuthal direction ' ϕ '. Any function $f(\phi)$ is expanded as a truncated Fourier series

$$f_M = \sum_{m=-M/2}^{M/2} b_m e^{im\phi}, \quad (19)$$

with b_m being approximated by a discrete transform:

$$b_m = \frac{1}{M\tilde{c}_m} \sum_{l=0}^{M-1} f_l e^{-im\phi_l}, \quad (20)$$

where $f_l = f(\phi_l)$, $\tilde{c}_{M/2} = \tilde{c}_{-M/2} = 2$, $\tilde{c}_m = 1$ ($m \neq M/2$), $\phi_l = 2\pi l/M$ and $l = 0, 1, \dots, M-1$. In the Fourier method the derivatives are obtained by simply multiplying the coefficients of the expansion by the spectral index:

$$\frac{d^l f}{d\phi^l} = \sum_{m=-M/2}^{M/2} m^l b_m e^{im\phi}.$$

Both the Chebyshev and the Fourier methods are implemented in the code 'Fast Fourier Transform program' in the appendix containing the details.

$$u_{\text{Fourier}}(x) = \sum_{m=-M/2}^{M/2} b_m e^{im\phi_m}$$

is not required, since each dimension is treated separately. At each collocation point x_j we assume

$$u(\phi, t) = \sum_{m=-M/2}^{M/2} b_m(t) e^{im\phi},$$

using the following substitution

$$\sum_{m=-M/2}^{M/2} b_m e^{im\phi} = \dots$$

where $\phi = \phi(x_j)$ is the azimuthal coordinate at the j -th collocation point x_j .

$$\frac{\partial u}{\partial \phi} = \sum_{m=-M/2}^{M/2} \dots$$

where

$$a_m(t) = \sum_{m=-M/2}^{M/2} b_m(t) e^{im\phi}$$

3.3 The Fourth Order Runge-Kutta Temporal Scheme

We have decided to use and implement a fourth order Runge-Kutta method for the time dependence of the equations, it has the advantage of being conditionally stable when used with the Chebyshev method, in contrast to the second order Runge-Kutta scheme (the leapfrog predictor-corrector scheme, Gottlieb, Orszag & Orszag 1981) which is unconditionally unstable. Furthermore, the fourth order Runge-Kutta time differencing method has been proven to be the most efficient of the many schemes considered for the Chebyshev method by Fulton & Schubert (1987a & b, see also Fulton 1993).

Equations (2) is re-written in the following short form

$$\frac{du}{dt} = F, \quad (22)$$

where F is the vector function $F = (F_1, F_2, \dots, F_N)^T$ and $F_i = \frac{\partial u}{\partial x_i}$ ($i = 1, \dots, N$) is the numerical derivative in the i -th dimension.

$$\begin{aligned} F_1 &= \frac{du}{dx_1} = \frac{du}{dt} \\ F_2 &= \frac{du}{dx_2} = \dots \end{aligned}$$

The time step, Δt , is given by

$$\Delta t = \frac{\Delta t_{\text{ref}}}{N},$$

where Δt_{ref} is the usual Courant-Friedrich-Lowey restricted time step and N is the number of collocation points.

$$\Delta t = \Delta t_{\text{ref}} \cdot \min \left(\frac{\Delta x_1}{\Delta u_1}, \dots, \frac{\Delta x_N}{\Delta u_N} \right)$$

Δu is the grid spacing in the radial dimension, $\Delta u = r_{\text{max}} - r_{\text{min}} / N$.

We found out that the fourth order Runge-Kutta method can perform with a time step $\Delta t \approx 0.9\Delta t_{\text{ref}}$, but in some cases best results are obtained

when $\Delta t \approx 0.5 - 0.7\Delta t$. While the second order Runge-Kutta method performs well with a much smaller time step $\Delta t \approx 0.2 - 0.3\Delta t$. Consequently the present fourth order Runge-Kutta method is up to ≈ 3 times faster than the second order scheme. This implementation, together with the modified Chebyshev differentiation method (Kosloff & Tal-Ezer 1993) made the present numerical code very fast and efficient. A second order Runge-Kutta method used with the usual Chebyshev method as the one-dimensional one described in Godor (1996) would be slower by a factor of ≈ 20 for $N = 64$.

3.4 The open boundary

In order to insure non-reflective boundaries and avoid numerical instabilities as well as viscously driven oscillations (Godor 1996a), the boundary conditions are imposed on the characteristics of the flow and not on the primitive variables.

3.4.1 The characteristic approach

The characteristic approach is directly related to the physical variables. Characteristics are curves in the domain that connect points of equal values of a dependent variable. In the case of hydrodynamic problems, the characteristic variables are the velocity components and the pressure. The characteristic model can now be represented by $\frac{dx}{dt} = f(x)$, where x is the vector of dependent variables and f is the vector of characteristic functions. The system for the characteristic components of the flow can be written (Tadmor & Yihui, 1987)

$$\frac{du}{dt} = u_x \frac{\partial u}{\partial x} + u_y \frac{\partial u}{\partial y} + f_u$$

$$+ \frac{\partial p}{\partial x} - u_x \frac{\partial u}{\partial x}^2 - u_x u_y \frac{\partial u}{\partial x} - u_y u_x \frac{\partial u}{\partial y} - u_y^2 \frac{\partial u}{\partial y} = 0 \quad (11)$$

$$\frac{dp}{dt} = u_x \frac{\partial p}{\partial x} + u_y \frac{\partial p}{\partial y} + f_p$$

where $u = (u_x, u_y)^T$ and p is the pressure. The characteristic equations are represented by $\frac{du}{dt} = f(u)$ and $\frac{dp}{dt} = f_p$. Consequently the dependent variables and the pressure are connected by the flow variables. The characteristic approach is a direct way to solve the hydrodynamic equations of motion and an algorithm is then solved for the dependent variables u_x, u_y . In the present work the equations are solved explicitly, consequently the solutions for u and p can be considered

as a rectification of the boundary conditions imposed directly on u and c (Gottlieb, Grunzburger & Turkel 1982).

$$\begin{aligned} c_{+} &= (c_{+})_e + \left[\frac{\Delta u}{2} + 2n \frac{\Delta c}{2} \right], \\ c_{-} &= (c_{-})_e + \left[\frac{\Delta u}{2n} + \frac{\Delta c}{2} \right], \end{aligned} \quad (25)$$

with

$$\rho = \frac{(mc)^2}{(n+1)K},$$

and $\Delta u = (u_{+})_e - (u_{-})_e$, $\Delta c = (c_{+})_e - (c_{-})_e$. The terms in the squared brackets (eq.25) are the rectification terms, where c denotes exact values from outside the boundary and c denotes computed values at the boundary.

3.4.2 The isothermal Case

In the isothermal case $\rho = \rho_0$ and $c = c_0$. Therefore the previous treatment is not valid and one needs to rewrite the equations for ρ and u . Namely

$$\frac{\partial \rho}{\partial t} = 0$$

$$\frac{\partial u}{\partial t} = 0$$

3.4.3 Isothermal

$$\frac{\partial x}{\partial t} + \Lambda \frac{\partial x}{\partial r} = 0 \quad (27)$$

where

$$x = (\rho, u_r)^T, \quad \Lambda = \frac{1}{c_0^2/\rho - u_r^2}$$

The matrix Λ is lower diagonal

$$S \bar{u} A S u = \begin{pmatrix} \delta \rho & 0 & 0 & \cdots & 0 \\ 0 & \delta u_1 & 0 & \cdots & 0 \\ 0 & 0 & \delta u_2 & \cdots & 0 \\ \vdots & \vdots & \vdots & \ddots & \vdots \\ 0 & 0 & 0 & \cdots & \delta u_N \end{pmatrix}$$

and

$$S = \begin{pmatrix} 1 & 0 & 0 & \cdots & 0 \\ 0 & 1 & 0 & \cdots & 0 \\ 0 & 0 & 1 & \cdots & 0 \\ \vdots & \vdots & \vdots & \ddots & \vdots \\ 0 & 0 & 0 & \cdots & 1 \end{pmatrix}$$

The matrix equation is then solved for the particular case $\delta x = (\delta \rho, \delta u_r)^T$, where $\delta \rho = \rho - \rho_0$ and $\delta u_r = u_r - u_{r0}$ and the index zero denotes the steady

state solution (or an approximation to it). The eigenvectors so obtained are

$$\begin{cases} \rho = \rho_0 + \frac{\varepsilon}{\gamma} (v_r - v_{r0}), & (I) \\ \zeta = (\rho - \rho_0) - \frac{\varepsilon}{\gamma} (v_r - v_{r0}), & (II) \end{cases} \quad (28)$$

The eigenvalues associated with the eigenvectors (I) and (II) are $v_r + c$, and $v_r - c$, respectively. When a characteristic (eigenvector) is incoming at a boundary, it is calculated using the exact value of the variable outside the boundary (the imposed physical boundary condition there); when a characteristic is outgoing, it is calculated using the computed values of the variables at the boundary. The imposition of the boundary conditions on the primitive variables (ρ, v_r) is carried out using the relations

$$\begin{cases} \rho = \rho_0 + \frac{D+H}{2}, \\ \zeta = v_{r0} + \frac{D-H}{2}. \end{cases} \quad (29)$$

These are taken by the primitive variables (ρ, v_r) at the outer boundary and are not explicitly stored (as was done in the original version of the code); the boundary fluxes are stored and allow the variables to take the values ρ_0 and v_{r0} at the outer boundary.

The present treatment of the boundary conditions has the advantage of being a simple and inexpensive way of dealing with the problem of non-reflecting boundary conditions (for a review see Givoli 1991; see also Al'fishat et al. 1991). The code was tested in one dimension, and the use of the above treatment prevented viscous oscillations to an extent that is better than any other (Givoli 1991). It is, however, important to remember that an approximation and in some case can lead to partial reflection of shocks. If this is the case, the algorithm automatically handles the shock, which has the effect of a disturbance well within the grid, thus bypassing an unnecessary and expensive treatment with $n_p = 1$.

4 Results and Discussions

We have tried and compared with different physical and numerical assumptions all the models presented below. We found that a high resolution was needed at the inner edge of the disc, while the outer edge was treated with a lower resolution. Best results (in speed, resolution and stability) were obtained by choosing $n_r = 9$ and $n_\theta = 2$ in the modified Chebyshev method

(see section 3.1). Some models, however, were run with $n_r = 5$, that is to say with a lower resolution in the inner part of the disc. Most of the models were run with $N = 64$ collocation ('grid') points in the radial direction and $M = 32$ points in the angular direction ($NNM = 64 \times 32$). Models with $M = 16$ developed numerical oscillations in the angular dimension in the outer part of the disc, due to the strong tidal coupling. In this region of the disc, shocks can form and the waves are non-linear and cannot be represented by simple sine functions, therefore justify in the choice $M = 32$ (a higher number of terms is needed in the Fourier expansion to represent the function). Models with $N = 64$ had to be run with $n_p = 2$, while models with $N = 128$ could be run with $n_p = 3$. The models we tried with $NNM = 128 \times 64$ and $NNM = 128 \times 128$ were extremely slow and could be run for only a few binary periods. Therefore, we decided to run mode's with 64×32 , which were faster by a factor of ≈ 100 .

We also checked the effect of the alpha viscosity parameter and the mass ratio a . Models with zero or unity ($\alpha = 0$ or $\alpha = 1$) viscosity parameters are hard to run for a long period of time without numerical instabilities. Models with $\alpha = 0.1$ developed strong shocks in the outer region of the disc and caused numerical oscillations. At $\alpha = 0.2$ the code worked well, but still had some numerical oscillations.

We chose $\alpha = 0.2$ for the present calculations, since $\alpha = 0.2$ is a good value and $a = 1.0 \times 10^{-3}$ ($\approx 10^3$). Since we are solving for a steady-state solution, we do not care about the numerical oscillations in the outer region of the disc, as long as we normalize ρ to unity (see for example Savonije et al. 1994). The unit of length is the inner radius of the computational domain ($R_{in} = 10$) and the unit of time is the orbital period of the binary. The computation time is set to be sufficiently large to ensure that the system is in equilibrium ($\approx 10^4$ units of time), as is commonly adopted by other authors. In all the modes $R_{in} = \dots R_{out} = 10$ and $a = 1.0$.

We have tried models with a uniform resolution of the outer region (uniform cell size Δr). The resolution Δr in the disc is a most important parameter in the increasing radius. However, it is important to note that at the outer boundary, the resolution Δr may be too large or too small. A small value of Δr will result in a poor representation of the outer boundary (see Cen et al. 1991), while a large Δr may cause numerical instabilities and numerical oscillations. Therefore, it is necessary to choose a reasonable value of Δr that is not too large or too small. This is done by trial and error. The best resolution is obtained when the outer boundary is placed far enough from the 'outer edge' of the disc, in which the disc has a given initial mass which increases due to the accretion process (such a disc never reaches steady state). In this case the outer boundary has to be placed far enough from the 'outer edge' of the

disc, to ensure that it does not affect the outer disc. We have run such models for protoplanetary discs, with a low Mach number hot disc. The density of the outer disc decreases dramatically and sharp transitions and shocks appear close to the inner 'high density cold' arms, which prevent us to run the spectral code for a long period of time. Spectral methods do not converge when a discontinuity forms in the variables or in their derivatives. Consequently, we have imposed the boundary condition on Ω itself at the outer boundary. Ω is the solution of the angular momentum equation when $a_0, v_0 \ll r_0$ (see section 2.3 equation 6). In this case the angular velocity profile is a smooth function which decreases monotonously outward ($\partial\Omega/\partial r < 0$). The angular momentum is then transported through the boundary due the negative torque at the boundary, whose value is obtained as a part of the numerical solution of the equations. In this case there is no artificial outgoing flux of matter.

4.1 Modeling the onset of the eccentric instability in SU-LVMe systems

In SU-LVMe systems, the eccentricity increases until it reaches a value of about 0.05, and the outer disc begins to become 'cold' when it loses angular momentum and the inner disc reaches the first resonance region. Local resonances can then induce perturbations along the disc, which can trigger the eccentric instability.

We consider a disc with a central point mass of a compact object with $\epsilon = 0.05$ at the outer radial boundary and the polytropic index is $n = 3$. The eccentricities are initialized to a value between $0.01 \leq e \leq 0.05$, in the range $2^{\circ} \leq \vartheta \leq 180^{\circ}$, through the disc's parameter of real discs found in LVMe.

Model 1: In this model $\epsilon = 0.05$ and $e = 0.02$. Within one binary orbital period, the eccentricity develops, changing its value from 0.02 to 0.05, and the disc becomes 'cold'. This is a typical example of the onset of the eccentric instability in a protoplanetary disc. The appearance of the eccentric instability is triggered by the resonance of the local radial mode, magnifying the angle of the outer disc, forming a spiral pattern, where the radial patterns are converging. This pattern has a characteristic wavelength λ_{c} . Small initial values of e and ω form a strong pattern in the outer disc, and decay on a slower timescale (van Gool et al. 1996a). The outer radial pattern oscillates slightly in the spatial dimension and the disc clearly appears to be unsteady. An eccentric ($m = 1$) mode develops

immediately in the very inner part of the disc. This eccentric mode is a high density crescent pattern which rotates in the inertial frame of reference, in the retrograde direction (figure 2), at a speed $\Omega_{\text{cres}} \approx 0.73\omega$ (in the rotating frame of reference one has $\Omega_{\text{cres}} \approx 1.73\omega$). The rotation period of the crescent appears to decrease slightly with time. As the crescent rotates it excites a wave which propagates outward and induces eccentricity in the outer region of the disc (figure 3). The $m = 1$ mode dominates the inner disc during the first binary orbits ($t \approx \text{a few } P_b$). At a time of about $t \approx 5$, an $m = 2$ mode appears in the inner part of the disc, characterized by an elliptic density pattern. The streamlines are actually elliptic in this region and the matter rotates at about the 'local' Keplerian velocity (figure 4). The ellipse processes in the prograde direction with a period $P_2 \approx P_b/13$ ($\Omega_2 \approx 13\omega \approx \Omega_b/3$). The $m = 1$ mode grows with time while the $m = 2$ mode slightly weakens. Eventually, the eccentric instability dominates the whole disc and strong shocks appear in the outer region (figure 5). We stopped the computations at $t \approx 35$ orbits, since the disc became numerically unstable due to the shocks.

As we are using a Fourier decomposition in the angular direction, it is useful to make a spectral analysis of the density. The Fourier decomposition is carried out in the rotating frame of reference of the binary orbit in the $x - r - \vartheta$ plane. The results are shown in figure 6, where we see the eccentricity and the ellipticity of the disc.

and we analyze the time dependence of the Fourier coefficients ' p_1^2 ' and ' p_2^2 ', which determines the growth rate of the eccentric and elliptic modes, respectively, at different radii in the disc. In figure 6a we show the time dependence of the $m = 1$ mode in the very inner part of the disc at $r = 1.01$, while the $m = 2$ mode is shown in figure 6b. Mode 2 grows rapidly during the first 10 orbits, and then stabilizes, while mode 1 grows more gradually during the disc period considered here. The $m = 2$ mode is independent of the rotation of the inner disc in elliptic orbits. The process has a very short duration of ≈ 10 orbits and then the disc becomes 'cold'. The outer disc, which has a fixed orbital motion, still has a constant rotation of the local Keplerian velocity, so the oscillations between mode 1 and 2 last until the resonance sets up again. At $t \approx 10$ orbits, we have $e \approx 0.05$ and $\omega \approx 0.05$ (see the SPH simulations of Murray 1995). The situation looks the same up to a radius of ≈ 1.5 . At larger radii the $m = 2$ mode has a constant value, while the $m = 1$ mode grows steadily (figures 7a and 7b, here $r = 3.2$). At this radius the $m = 2$ mode is characterized by the spiral pattern with no elliptic

orbits. With time the $m = 1$ mode increases and becomes comparable to the $m = 2$ mode, which grows unsteady. In figure 7c we show the frequency decomposition (a discrete Fourier transform in time from $t \approx 10$ to $t \approx 35$, with 1024 terms and $\Delta t = 1/32P_0$) of the $m = 2$ mode which shows two strong peaks at $\Omega \approx 1.7\omega$ and $\approx 3.4\omega$. The 1.7ω frequency is the frequency of the eccentric ($m = 1$) rotating crescent. The 3.4ω frequency is the first harmonic of the 1.7ω frequency, and is probably due to coupling of the 1.7ω frequency with the $m = 2$ (symmetric) mode. The other peaks are very weak (the scale is logarithmic) and are probably stroboscopic effects, since the time resolution is low. At larger radii the situation is quite the same, except for viscous oscillations, close to the outer boundary, which pollute the modes during the first 10 binary orbits. In figure 8 we show a graph of the ratio ρ_2'/ρ_1' (in arbitrary units) at five different radii. By $t = 35$ orbits the $m = 1$ mode is comparable to the $m = 2$ mode.

Model 2 In this model we choose a small inner gap ratio $a = 0.01^2$ and repeat the simulation of $a = 0.1$. A similar wave pattern develops with a longer timescale, because in the outer disc a stronger outward pressure gradient is established (sheath resonance). The disc seems to find a new steady state during the first 20 binary orbits. After this, the disc becomes more and more unstable, due to the growth of some of the modes. In particular, an $m = 2$ mode appears in the outer disc around $t = 30$. This mode rotates processes in the prograde direction with a period P_2 which is a fraction of the binary period but which is longer than the 'local' Keplerian period. In the rotating frame of reference one has $P_2 \approx P_0/6.2$ or $P_2 \approx Q_{\text{loc}}/6.2$. The frequency spectra of the mode 2 at $t = 21$ reveals in figure 9 a single peak around ω . At a later time ($t \approx 35$), the $m = 1$ mode develops as a rotating crescent. It rotates in the 'internal' frame of reference with an azimuthal frequency $\Omega \approx 1.5\omega$ (which is 1.5 times higher than the external Keplerian rotation $\Omega \approx 1.5\omega$). This is a typical resonance for the regular Roche-lobe overflow. We note that the $m = 1$ mode grows at a constant rate, while the $m = 2$ mode, which has a $m = 1$ mode waveform, is by far the one that grows faster. In particular, at $t = 35$, the $m = 1$ mode decreases rapidly and reaches a plateau, while mode 2 grows much rapidly. Figure 10 shows the growth rates of $m = 1, 2$, which is again similar to the growth rates of model 1. Model 1 becomes the dominant mode around $t \approx 60$ orbits (figure 12). The computations were stopped around $t \approx 70P_0$, due to strong shocks.

Model 3 This model is the same as model 1, but with a different boundary conditions. In model 1 and 2 the outer boundary condition is a constant steady inflow $U_{\infty} = \rho_{\infty} c = U_{\text{in}}$. Since the conditions are imposed on the characteristics, the actual value of U at the boundary differs from the computations shows that $U \approx U_{\infty}$ mainly at the location of the spiral pattern, which means that the matter is accreted mainly through the spiral. In the present model we impose $U_{\text{in}} = 0$. This condition is stronger than the previous one, in the sens that the actual value of U (obtained in the computations) at the boundary is $U \approx 0$ everywhere at the outer boundary. In this case there is no inflow of matter and the quantity of matter in the disc is kept constant ($M = 0$ at the inner boundary too). Since the matter is slowly accreted in the disc one expect the radius of the disc to decrease with time and eventually the the disc becomes 'too small' to interact tidally with the companion. However, the boundary condition does not seems to affect the evolution on a small time scale overwhich the models are run; this model is also stopped at $t \approx 70P_0$.

Model 4 This model is the same as model 1, but with a different initial condition. We have chosen to use the same initial condition as in model 1, but with another starting matter profile in the inner disc. In this model the outer disc is initially empty. The disc is then formed by an inward moving wave, which propagates from the outer edge of the inner disc. The density profile of the inner disc is shown in figure 11. The density contrast is smaller than in model 1, and the density profile is more uniform. The density profile in the outer region of the disc (this pattern is seen only after enhancing the density contrasts with the color effect).

4.2 Modeling discs in Young Stellar Objects

In NSO's the situation is quite a bit simpler than in the previous cases, because the outer disc is not an open accretion object. In this present work we consider only the outer region of the disc (inner disc, the orbit of the star, the outer disc). The mass of the disc is constant, and it is in quasi-equilibrium. The outer disc has a rotation frequency $\Omega = 1/10P_0$. We assume $c = 0$ for the disc (neglecting rotation). As in section 4.1, we choose $a = 0.1$, and we choose the outer radius of the disc to be $10R_{\odot}$. The code was computed for the outer disc using $n \gg 1$, and gave the same results. The outer disc is assumed such that the Mach number in the disc is small (less than 10), as is usually not disc found in NSOs. Consequently, the shear pattern is more 'open' and winds up only a few times before it reaches the lower edge of the disc. Here we impose a zero mass inflow condition at the outer radial

Nov. 5 The first ground test was performed at the same site as the previous one, but with the following differences. First, the ground was leveled and made smooth. Second, the source was moved more than 100 m from the center of the model's edge so that the source is much more "old" (fig. 13), and therefore it is reflected outward almost immediately by the inner edge of the disc. When it is reflected outward, the incoming and outgoing surface waves interfere with each other and form standing surface waves. This pattern is shown for about an hour. After this time interval the waves become rapidly with time and the character of the standing wave changes around ≈ 10 min (fig. 13). $\delta V \approx 10$ – 15 m. The variation of the inner boundary is asymmetric, and the variation of the outer boundary is symmetric.

W. H. Dickey, who is a member of the Board of Education, has been elected to the State Board of Education. He was elected by the Board of Education at their meeting on May 20, 1914.

卷之三

the original study, the mean age was 22 months for both groups. The mean age at the time of the second study was 36 months. The mean age at the time of the third study was 42 months. While no data is available on the growth of children in the reference cohort, our data (Korsham et al., 1993) were interesting to compare to the original study. At 36 months, the mean height in the reference cohort was 105 cm, the mean weight was 18 kg, and the mean head circumference was 51.5 cm.

which propagates to small radii. It is not clear however how the boundary layer would interact with the spiral density waves and how the waves would be reflected. In both cases, one would need to carry out two-dimensional simulations of non-axisymmetric boundary layers, in order to assess the effect of tidal forces on the boundary layer.

Acknowledgments

This work was performed while the author held a National Research Council - (NASA Jet Propulsion Laboratory) Research Associateship. This research was carried out at the Jet Propulsion Laboratory, California Institute of Technology, under contract to the National Aeronautics and Space Administration.

References

- Ababouche S., Don W.S., Gottlieb D., Rudy O.H., Townsend J.C., 1991, *J. Fluid Mech.*, 225, 557

 2. Caflisch C., Hussaini M.Y., Quarteroni A., Zeng C.A., 1988, *Spectral Methods in Fluid Dynamics*, Springer Verlag, New York, Berlin.
 3. Fulton, S.R., 1993, *J. Comput. Phys.*, 126, 299
 4. Fulton, S.R., Schubert, W.H., 1987a, *Mon. Weather Rev.*, 115, 1940
 5. Fulton, S.R., Schubert, W.H., 1987b, *Mon. Weather Rev.*, 115, 1953
 6. Givoli, D., 1991, *J. Comput. Phys.*, 94, 1
 7. Godunov, S., 1965, *VNPAS*, 274, 61

Table 1. Summary of the results of the 1993 survey.

8

9. Gottlieb, S., & Orszag, S.A., 1977, *Numerical Analysis of Fourier Series and Integral Representations*, McGraw-Hill, New York, NY.

10. Gottlieb, S., & Orszag, S.A., 1983, *Numerical Analysis*, Academic Press, New York.

11. Gottlieb, S., Gorenflo, M., & Tuckwell, H., 1982, *SIAM J. Numer. Anal.*, volume No. 19, p. 1.

series on nonuniform phenomena in stellar atmosphere, NASA SP-597.

12. Gottlieb, S., Gorenflo, M., & Tuckwell, H., 1982, *J. Math. Phys.*, volume No. 23, p. 1.

13. Gottlieb, S., Gorenflo, M., & Tuckwell, H., 1982, *J. Math. Phys.*, volume No. 23, p. 2.

14. Gottlieb, S., Gorenflo, M., & Tuckwell, H., 1982, *J. Math. Phys.*, volume No. 23, p. 3.

15. Gottlieb, S., Gorenflo, M., & Tuckwell, H., 1982, *J. Math. Phys.*, volume No. 23, p. 4.

16. Gorenflo, R., A. Isayev, M. Wolfson, V. Orlitzky, *Chaos-dynamic Variables*, Kluwer Academic Publishers, Dordrecht, The Netherlands, p. 329.

18. Lubow S., 1991, ApJ, 381, 298
19. Lubow S.H., 1992, in W.J. Duschl, J. Frank, F. Meyer, E. Meyer-Hofmeister, W.M. Teukolsky (eds.), Theory of Accretion Disks-2, Kluwer Academic Publishers, Dordrecht, The Netherlands, p.109
20. Murray J.R., 1996, MNRAS, 279, 402
21. Osaki Y., 1993, in W.J. Duschl, J. Frank, F. Meyer, E. Meyer-Hofmeister, W.M. Teukolsky (eds.), Theory of Accretion Disks-2, Kluwer Academic Publishers, Dordrecht, The Netherlands, p.93
22. Papaloizou J.C.B., Stanley G.Q.G., 1986, MNRAS, 220, 253
23. Pringle J.E., 1994, in W.J. Duschl, J. Frank, F. Meyer, E. Meyer-Hofmeister, W.M. Teukolsky (eds.), Theory of Accretion Disks-2, Kluwer Academic Publishers, Dordrecht, The Netherlands, p.55

© 0000 RAS, MNRAS 000, 000-000

REFERENCES AND NOTES

Received: 0000-00-00; Accepted: 0000-00-00

MNRAS 000, 000-000

© 0000 RAS, MNRAS 000, 000-000
Journal of Computational Mathematics, M23, 1998, Special Number on Partial Differential Equations, ©SIAM-CRVS, distributed by SIAM

ISSN 1064-8228/98/020001-13\$15.00 © 1998 Society for Industrial and Applied Mathematics

24. Lubow S.H., 1994, in W.J. Duschl, J. Frank, F. Meyer, E. Meyer-Hofmeister, W.M. Teukolsky (eds.), Theory of Accretion Disks-2, Kluwer Academic Publishers, Dordrecht, The Netherlands, p.109

Figures caption

Figure 1. A grayscale of the log of the density is shown for model 1. High density is dark and low density is clear in the rotating frame of reference of the binary. The inner radius is $R_{in} = 1$ and the outer radius is $R_{out} = 5$. The secondary object is located to the right at $r = 12$, and has a mass $m = 0.08 \times M$. The double spiral pattern (characteristic of the 2:1 resonance) is tightly wound-up, since the disc is cold.

Figure 2. Grayscale of the density for mode 1. The $m=1$ mode is shown in the inner part of the disc, in the rotating frame of reference. The mode is characterized by a crescent shape rotating in the retrograde direction (relative to the inertial frame of reference). The rotation rate decreases with time.

Figure 3. Grayscale of the momentum $H = pr$ is shown for model 1. Negative values (directed inward) are dark and positive values (directed outward) are clear. A shear wave propagates outward (white spiral pattern) from the inner edge of the disc, and reaches about $r = 15$ at the outer edge of the disc. The transient compression rapidly develops in a thin plume near the outer edge, the angular frequency was taken to be $\omega = 2\pi/3$.

Figure 4. Grayscale of the density for model 1. The inner region of the disc is shown in the rotating frame of reference, not with the content of Figure 1. The density is high in the inner region, and decreases rapidly towards the outer edge of the inner disc. An elliptic ($m=2$ mode) high density pattern has developed adjacent to the inner boundary. The elliptic mode amplitude increases at a rate faster than the binary rotation but slower than the local Keplerian velocity.

Figure 5. Grayscale of the density for model 1. The inner region of the disc after the transient compression of Figure 4 has transformed into a more elliptically shaped region and forms a pair of lobes (left and right). The inner region has a higher density than the outer region. The angular frequency was taken to be $\omega = 2\pi/3$.

Figure 6. The 'The Eccentricity' (1) of the density is drawn. It is plotted in 'inertial units' as a function of time (in units of the orbital period of the binary). It shows the growth rate of the eccentric $m=1$ mode ($m=1$ in model 1). The eccentric mode grows gradually and becomes comparable to

the elliptic mode (figure 6b) around $t = 30$.

Figure 6b. The Fourier coefficient $|\rho_2^2|$ of the density is drawn as a function of time. It shows the growth rate of the elliptic $m = 2$ mode at $r = 1.0$ in model 1. The elliptic mode grows rapidly during the first 10 orbits and is characterized by an elliptic high density pattern (figure 4).

Figure 7a. The Fourier coefficient $|\rho_1^2|$ of the density is drawn as a function of time, at $r = 3.2$ in model 1. The eccentric mode grows gradually and becomes comparable to the elliptic mode (figure 7b) around $t = 25$.

Figure 7b. The Fourier coefficient $|\rho_2^2|$ of the density is drawn as a function of time, at $r = 3.2$ in model 1. The elliptic mode does not grow, and is characterized by the double spiral pattern in the density (figure 1).

Figure 7. The time dependence of the Fourier coefficients of figure 5 has been decomposed into a spectrum of frequencies (in units of $1/\Omega$, the period of one complete orbit). A peak around $1/2$, the frequency of the eccentric mode, corresponds to $m = 1$ mode, and $m = 2$, which is the elliptic mode. The density pattern is characterized by a double spiral pattern (figure 1), while the elliptic mode is characterized by an elliptic high density pattern (figure 4).

Figure 8. The ratio of the eccentric mode to the elliptic mode, $|\rho_1^2|/|\rho_2^2|$ (in arbitrary logarithmic units) is shown as function of time at five different radii in the disc for model 1. The radius $r = 5$ is shown at $y = 0$, $r = 4.3$ is at $y = 1$, $r = 3.2$ is at $y = 2$, $r = 2.1$ is at $y = 3$, $r = 1.0$ is at $y = 4$. The ratio of the eccentric mode to the elliptic mode decreases outward in the inner disc, and increases outward in the outer disc. The eccentric mode grows and becomes comparable to the elliptic mode around $t = 30$.

Figure 9. The Fourier coefficient $|\rho_1^2|$ and $|\rho_2^2|$ of the density is drawn in arbitrary logarithmic units as a function of time in units of the orbital period of the binary. It shows the growth rate of the eccentric ($m = 1$) and elliptic ($m = 2$) mode at $r = 1.0$ in model 2. The elliptic mode grows rapidly during the first 10 orbits and is characterized by an elliptic high density pattern. The eccentric mode grows gradually and becomes comparable to the elliptic mode around $t = 30$.

Figure 10. The Fourier coefficient $|\rho_1^2|$ and $|\rho_2^2|$ of the density is drawn (in arbitrary logarithmic units) as a function of time (in units of the orbital

period of the binary). It shows the growth rate of the eccentric ($m = 1$) and elliptic ($m = 2$) modes at $r = 2.1$ in model 2. The elliptic mode is rather steady, while the eccentric mode grows gradually and becomes comparable around $t = 30$.

Figure 11. The time dependence of the Fourier coefficient $|\rho_1^2|$ of figure 10 has been decomposed into a spectrum of frequencies (in units of $1/\Omega$, the amplitude is in logarithmic units). A sharp peak is seen around $1/2$, which corresponds to the frequency of the precessing elliptic pattern in the inner disc.

Figure 12. The ratio of the elliptic to the eccentric mode, $|\rho_2^2|/|\rho_1^2|$ (in arbitrary logarithmic units) is shown as function of time at five different radii in the disc for model 2. The radius $r = 5$ is shown at $y = 0$, $r = 4.3$ is at $y = 1$, $r = 3.2$ is at $y = 2$, $r = 2.1$ is at $y = 3$, $r = 1.0$ is at $y = 4$. The ratio of the eccentric mode to the elliptic mode decreases outward in the inner disc, and increases outward in the outer disc. The eccentric mode grows and becomes comparable to the elliptic mode around $t = 30$.

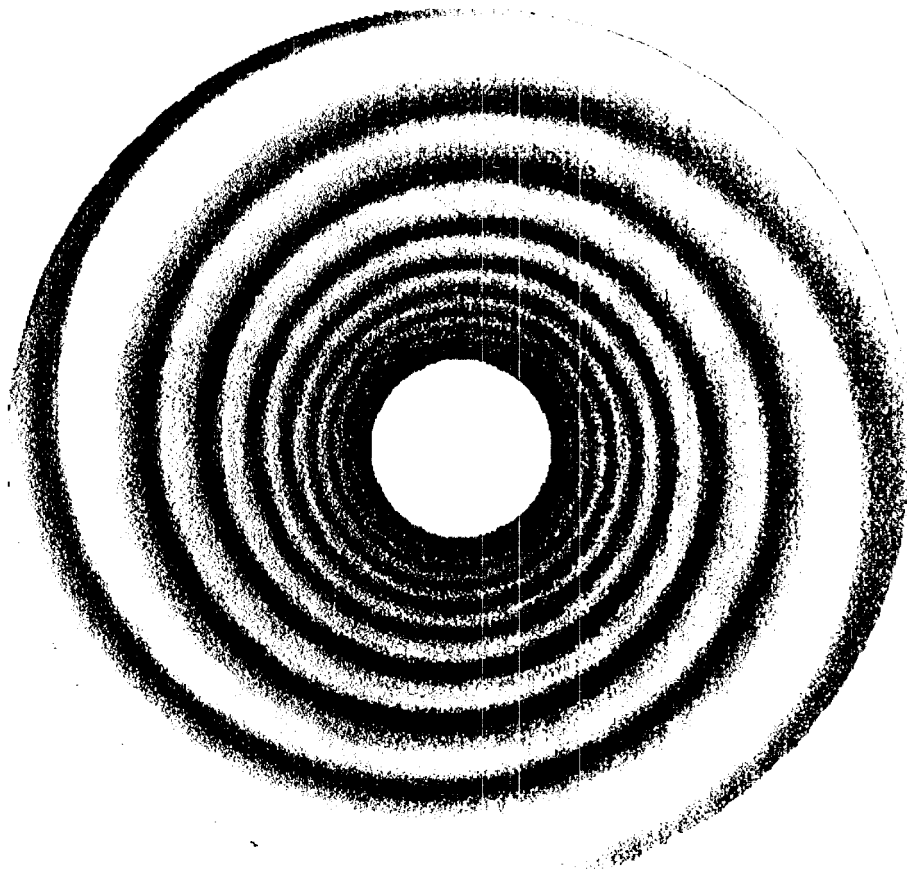
Figure 13. The orbital elements of the inner disc for model 2 are shown as function of time. The eccentricity e decreases from 0.5 to 0.2, the inclination i increases from 0 to 30°, and the longitude of the periastron ω decreases from 0 to 180°. The semi-major axis a remains constant at $a = 1.0$.

Figure 14. Grayscale of the density is shown in the inner disc for model 2. The reflected spiral wave interacts with the propagating wave, and forms standing waves.

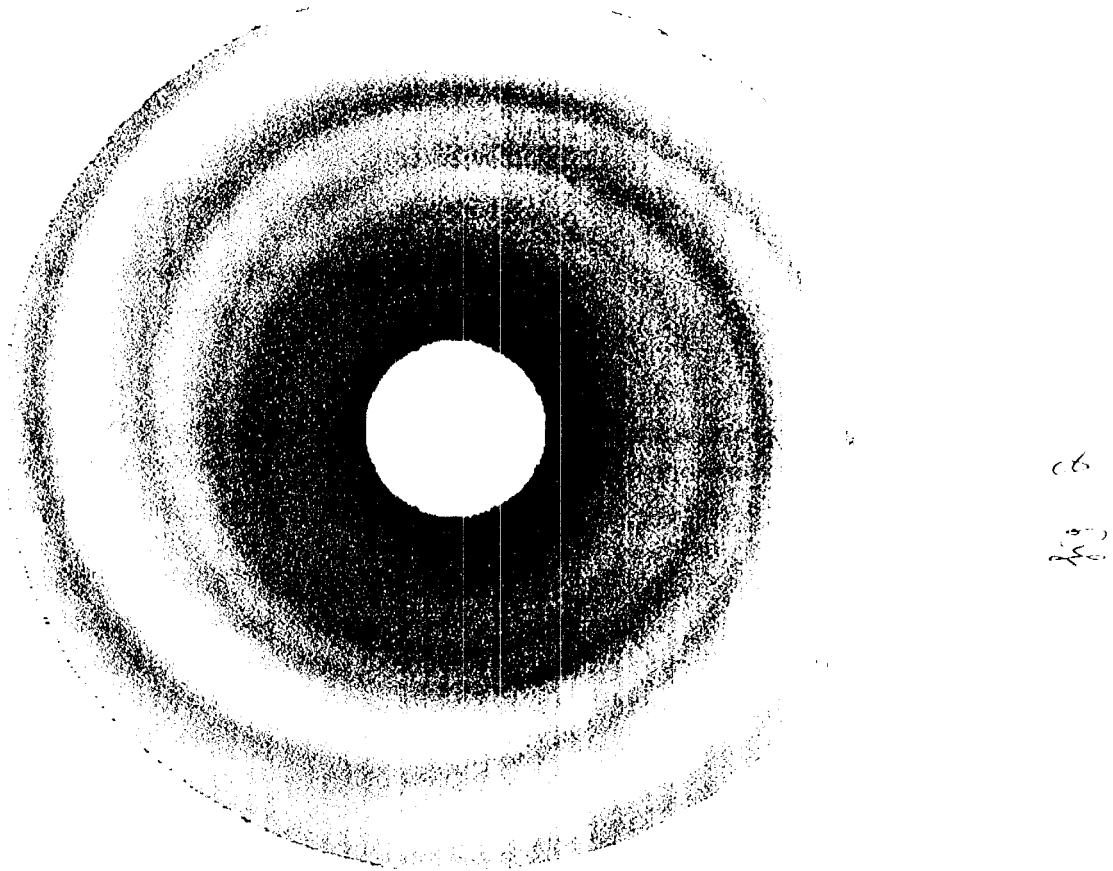
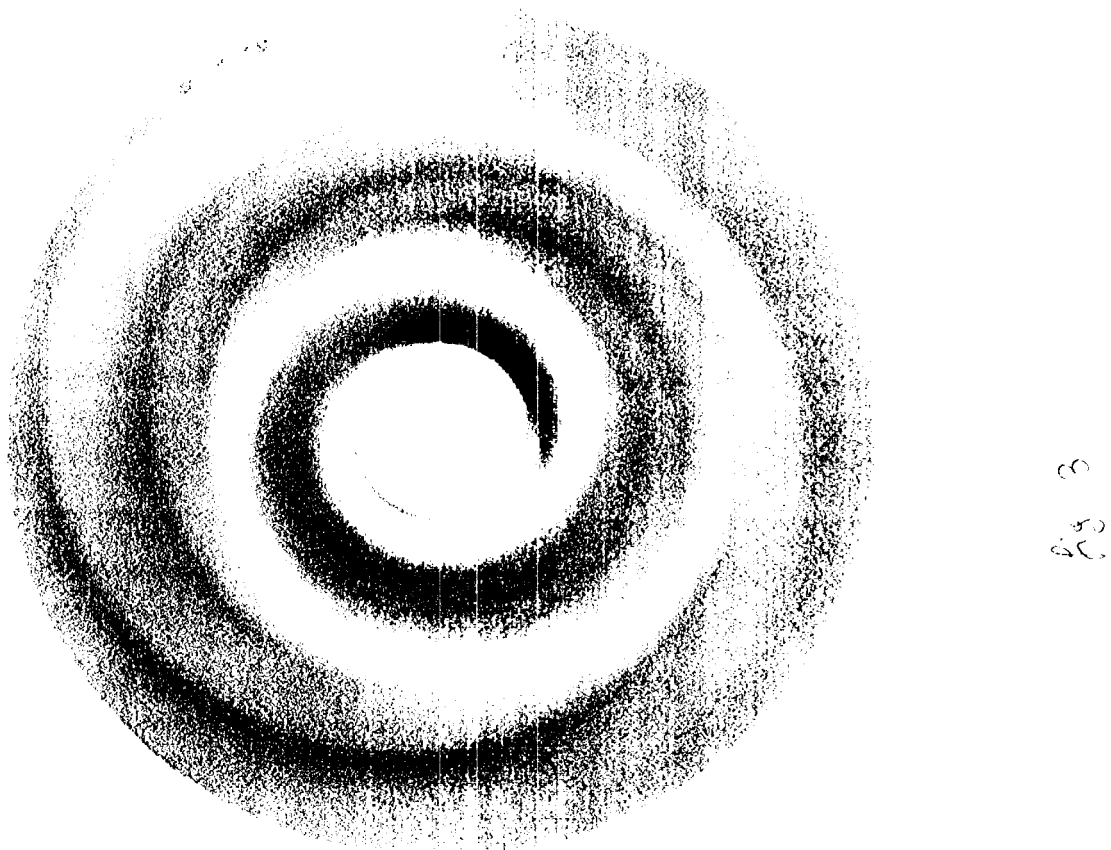
Figure 15. The minimum and maximum values of the density in the inner disc, showing the frequency of the density oscillations. The density is shown in arbitrary logarithmic scale, and the plot of the density is shown in grayscale. A sharp minimum occurs around $t \approx 10$ as the density is perturbed initially.

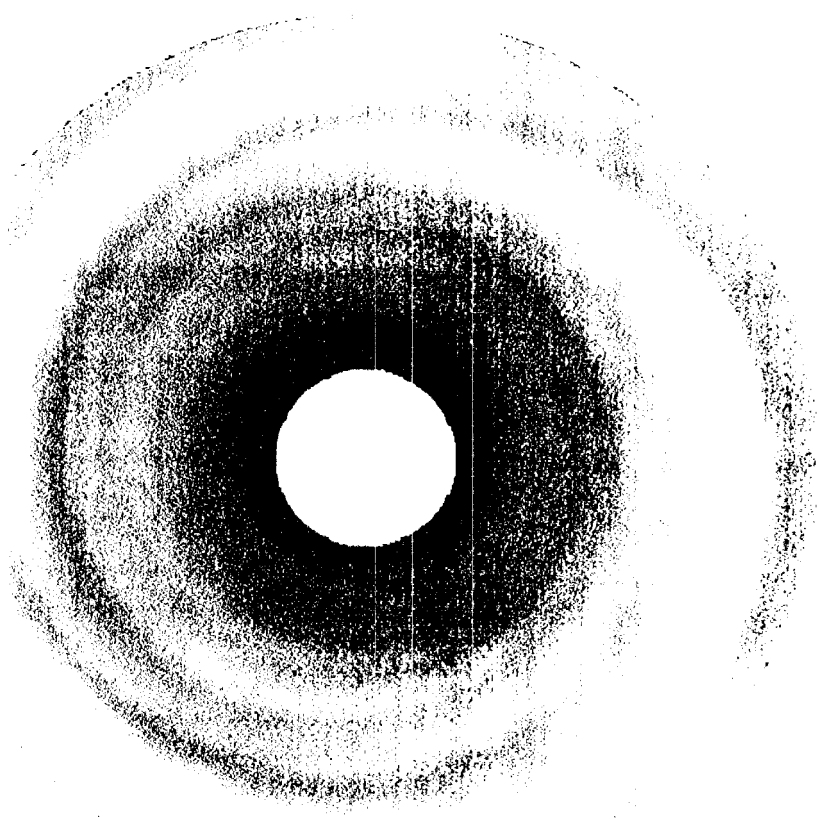
Figure 16. The evolution of the density in model 2 is shown at $t = 0$ and $t = 7$ orbital periods in units of the orbital period of the inner disc. The density is shown in grayscale. A rotating $m = 2$ mode located at the inner boundary induces weak spiral pattern in the inner region of the disc.

Figure 17a. The $m = 1$ mode ($|\rho_1^2|$ at $r = 1.0$) is shown as a function of time for model 2. A sharp transition occurs around $t \approx 10$ as the density



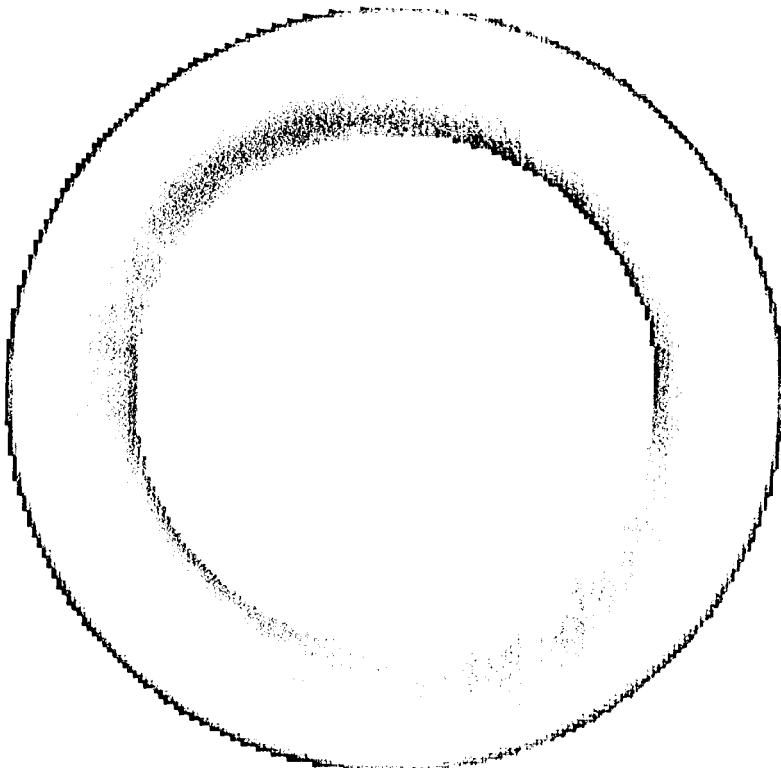
1
2





15

320

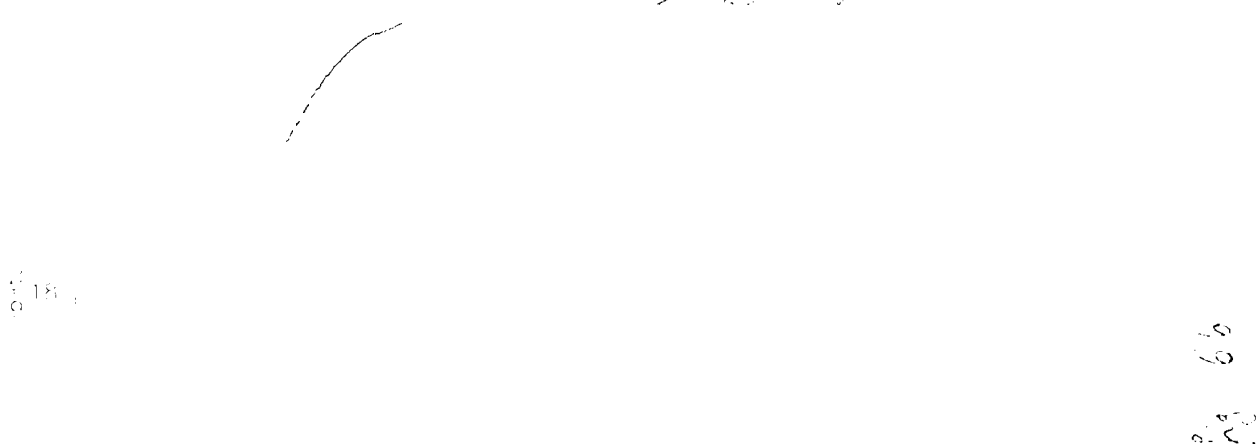


3

32

Electrolytic Method

Electrolytic Preparation of Fe_3O_4



Electrolytic Preparation of Fe_3O_4

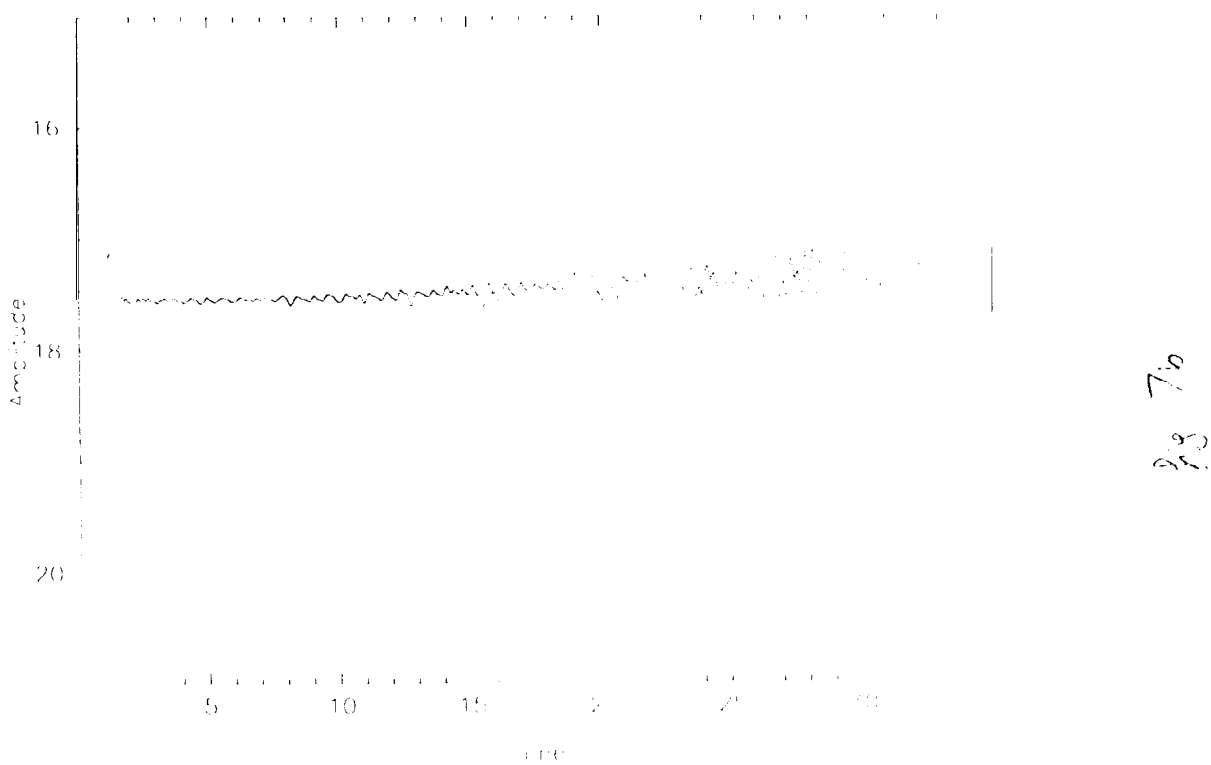
(100)



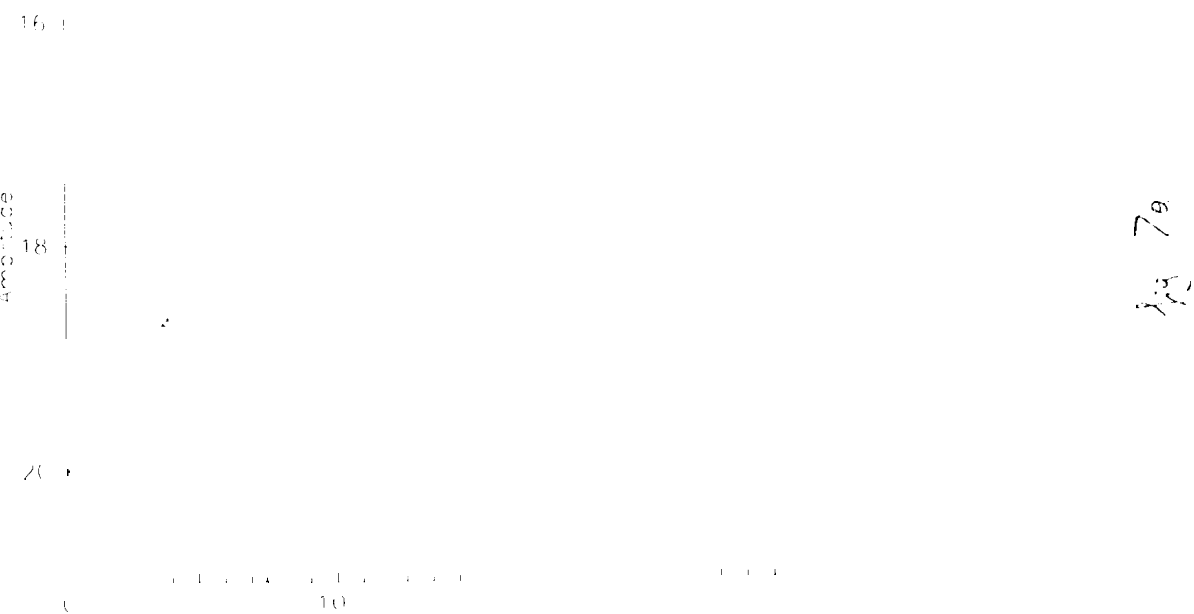
(100)

Electrolytic Preparation of Fe_3O_4

Fourier - II - unit



Fourier - ordene II



1970-1971

1970-1971

1970-1971

1970-1971

1970-1971

1970-1971

1970-1971

1970-1971

1970-1971
10

1970-1971

1970-1971

1970-1971

2

1970-1971
4

6.1

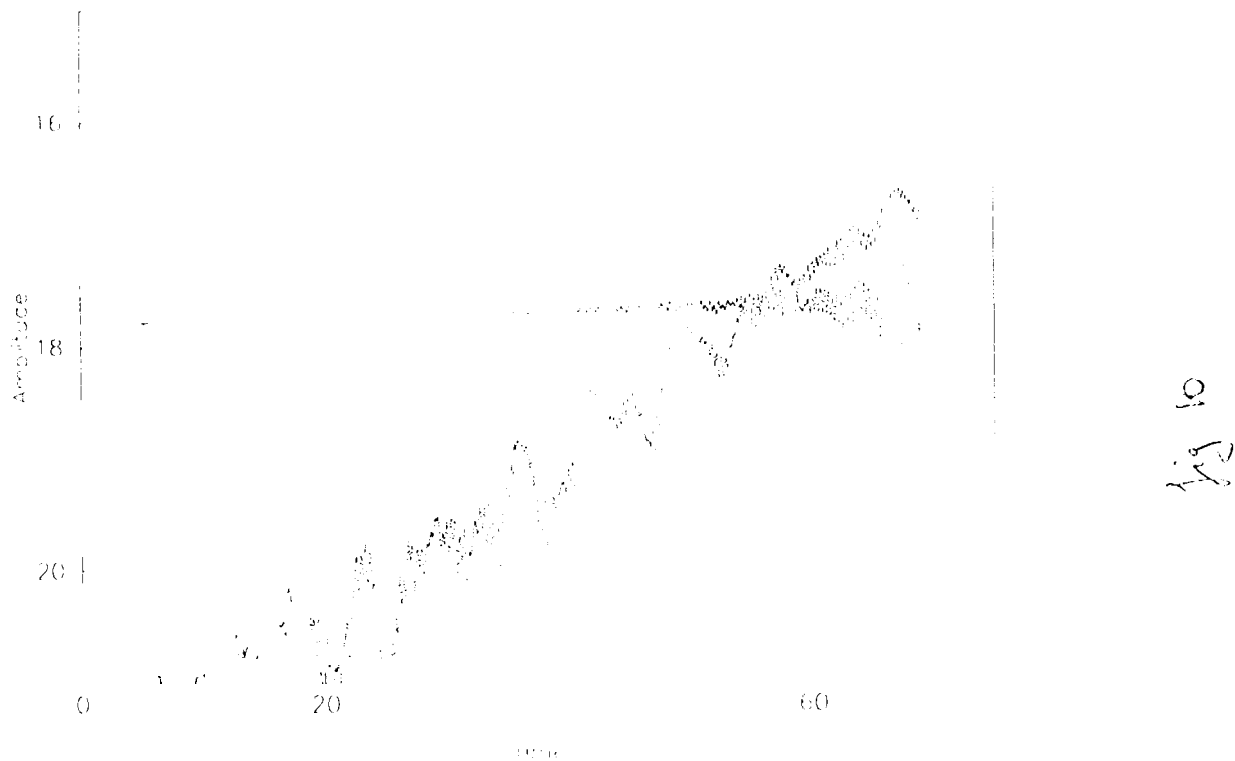
1970-1971
6.5

8.1

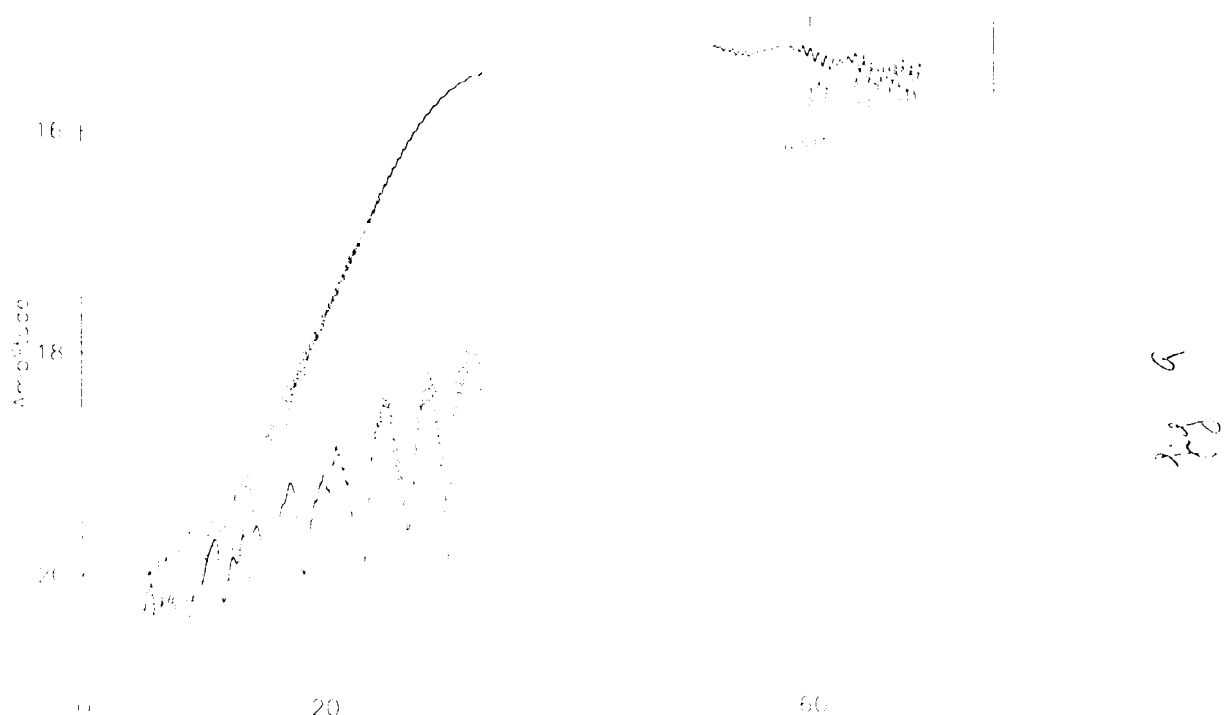
1970-1971
5

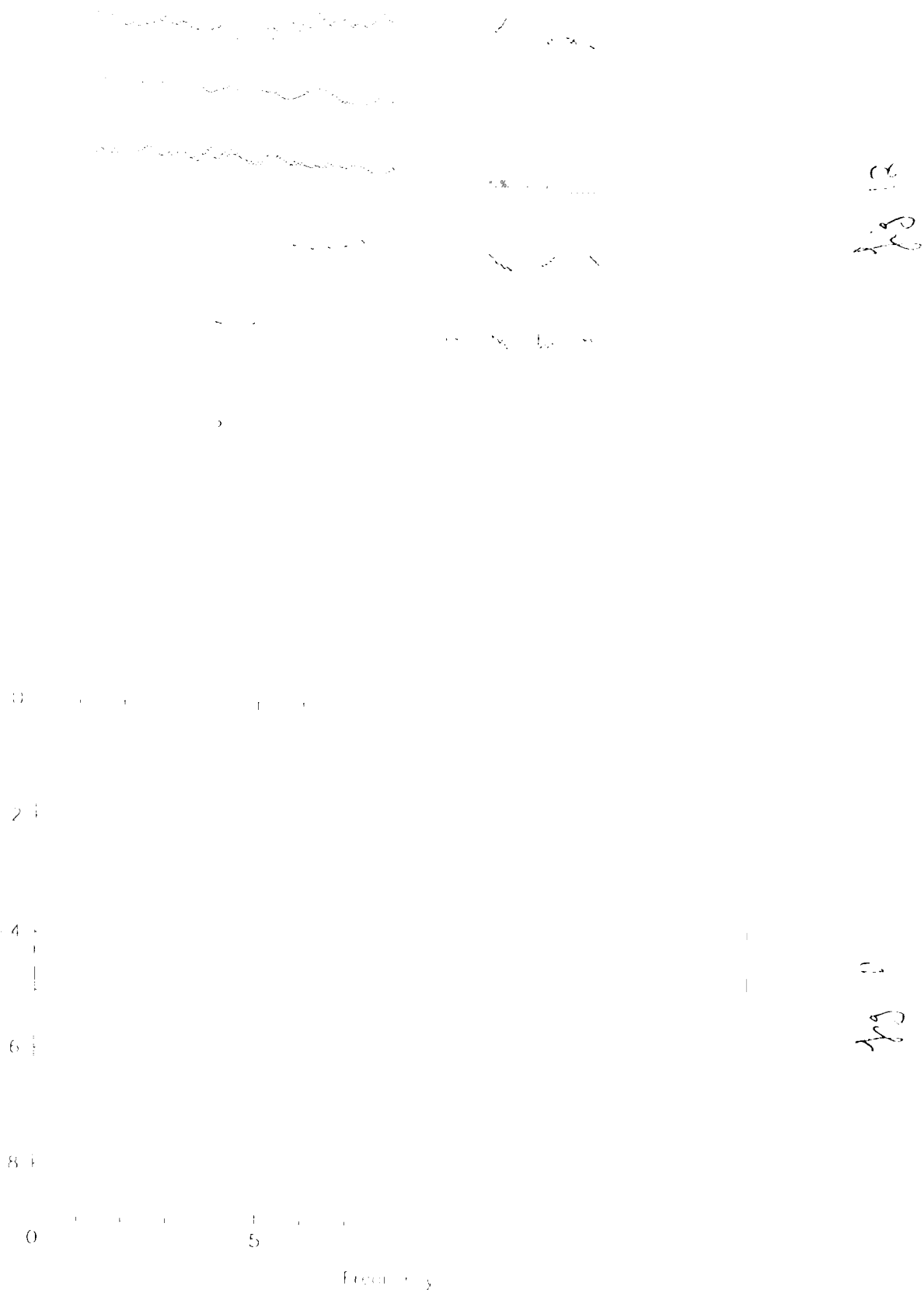
Freeze

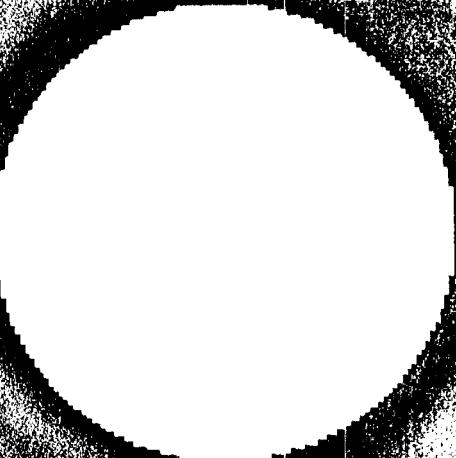
Fourier coefficient



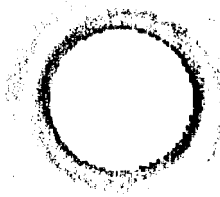
Fourier coefficient







119 14



119 3

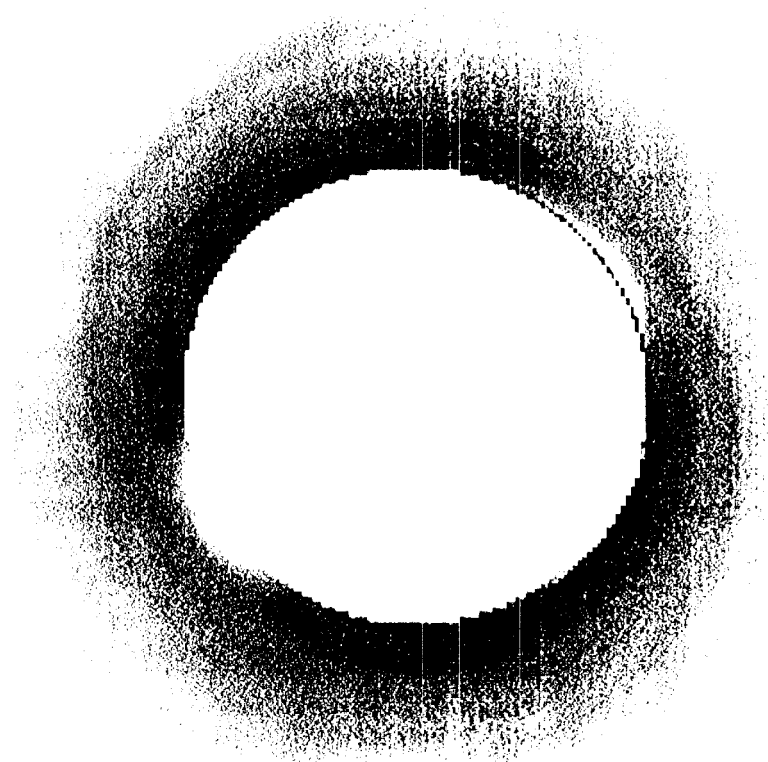
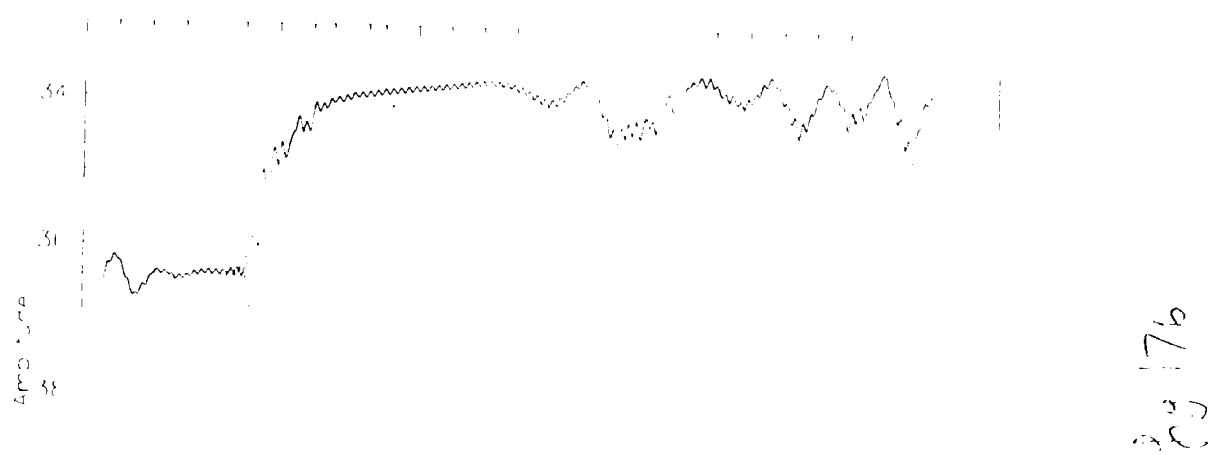


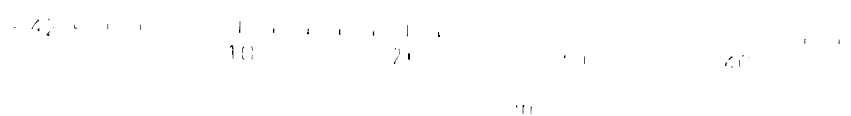
Fig 15

Fig 15

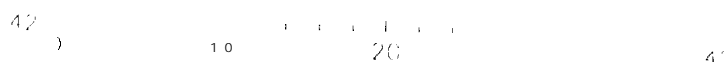
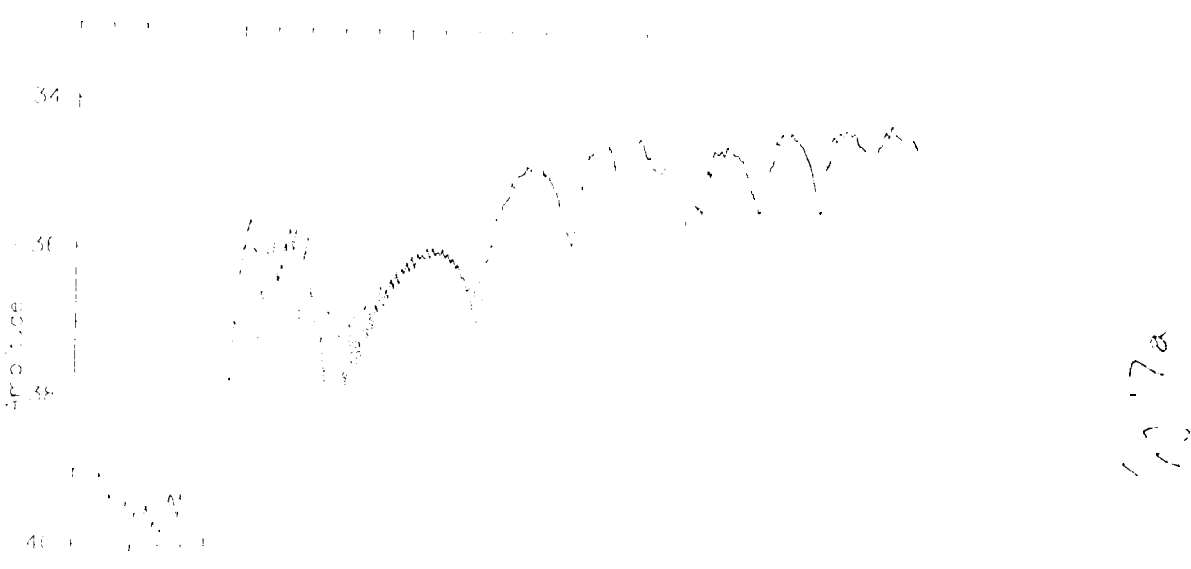
Fourier coefficient



40



Fourier coefficient



Fourier

Time (min)

30

30
35
40
 Σ_{d}

decreasing amplitude of oscillations, decreasing frequency of oscillations

40

35

35

42

10 20

t₁

Fourier transform

Time (min) 0 10 20 30

54

36
38
40

18a

15b

42

0

10 20

t₂

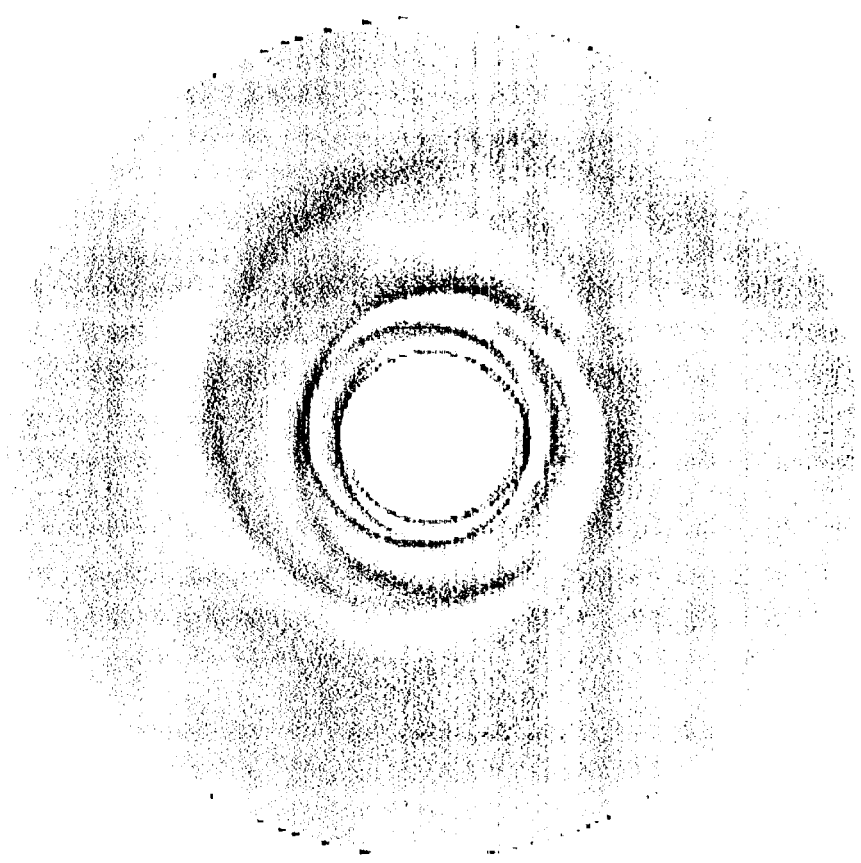


Fig 15